remote sensing

MDPI

Article

Change Detection of Small Water Bodies in Alluvial Gold Mining Satellite Imagery

Seda Camalan[1,*], Kangning Cui [2], Victor Paul Pauca[1], Sarra Alqahtani[1], Miles Silman[3, 4], Raymond Chan[2], Robert James Plemmons[1], Evan Nylen Dethier[5], Luis E. Fernandez[4], David Lutz[5]

[1] Department of Computer Science, Wake Forest University, Winston-Salem, NC USA 27109; camalas@wfu.edu (S.C.); paucavp@wfu.edu(V.P.P.); alqahtas@wfu.edu (S.A.); plemmons@wfu.edu (R.J.P.)
[2] Department of Mathematics, City University of Hong Kong, 83 Tat Chee Ave, Hong Kong; kangnicui2-c@my.cityu.edu.hk (K.C.); raymond.chan@cityu.edu.hk (R.C.)
[3] Department of Biology, Wake Forest University, Winston-Salem, NC USA 27109; silmanmr@wfu.edu
[4] Center for Energy, Environment and Sustainability, Wake Forest University, Winston-Salem, NC USA 27109; silmanmr@wfu.edu (M.S.); fernanle@wfu.edu (L.E. F.)
[5] Environmental Studies Department, Dartmouth College, Hanover, NH USA 03755; evan.Nylen.Dethier@dartmouth.edu (E.N.D.); David.A.Lutz@dartmouth.edu(D.L.);
* Correspondence: camalas@wfu.edu; Tel.: +1 (336) 758-5153

Abstract: Monitoring change of the land surface and within open water bodies is critical for natural resource management, conservation, and environmental policy. While the use of satellite imagery for these purposes is common, fine-scale change detection can be challenging due to the effects of atmospheric conditions on spectral data as well as the difficulty of connecting pixels to represent individual objects. We examined the degree to which two machine learning approaches can better characterize change detection in the context of a current conservation challenge, artisanal-scale gold mining (ASGM). We obtained Sentinel-2 imagery and consulted with domain experts to construct an open-source labeled land-cover change dataset for the Madre de Dios (MDD) region in Peru, a hotspot of ASGM activity, as well as in active ASGM areas in other countries (Venezuela, Indonesia, and Myanmar). With these labeled data, we utilized a supervised (E-ReCNN) and semi-supervised (SVM-STV) approach to study binary and multi-class change within mining ponds in the MDD region. Additionally, we tested how the inclusion of multiple channels, histogram matching, and La*b* color metrics improved performance of the models and reduced the influence of atmospheric effects. Our empirical results show that the supervised E-ReCNN method on 6-Channel histogram matched images generated the most accurate detection of change not only in the focal region (Kappa: 0.92(±0.04), Jaccard: 0.88(±0.07), F1:0.88(±0.05)) but also in the out-of-sample prediction regions (Kappa: 0.90(±0.03), Jaccard: 0.84(±0.04), and F1: 0.77(±0.04)). While semi-supervised methods did not perform as accurately on 6- or 10-channel imagery, histogram matching and the inclusion of La*b* metrics generated accurate results with low memory and resource costs. Altogether, we show how E-ReCNN is capable of accurately detecting specific and object-oriented environmental change related to ASGM, is scalable to areas outside our focal area, and is a method of change detection that can be extended to other forms of land-use modification.

Keywords: Change detection; small water bodies; ASGM, satellite image; deep learning; LSTM; smoothed total variation; SVM; semi-supervised;

Citation: Lastname, F.; Lastname, F.; Lastname, F. Title. *Remote Sens.* **2021**, *13*, x. https://doi.org/10.3390/xxxxx

Academic Editor: Firstname Lastname

Received: date
Accepted: date
Published: date

1. Introduction

Alluvial gold mining, frequently incorporated in the umbrella term artisanal scale gold mining (ASGM), is an emerging threat to the conservation and preservation of tropical riverine systems across the planet [1,2]. This method of mining involves the removal of aboveground biomass and the processing of alluvial soil sediments for the retrieval of minute historical deposits of gold particles. ASGM typically involves operations at a much broader spatial scale than pit mining, as the concentration of gold particles is comparatively low in alluvial fans and historical river channels [3]. As a result, ASGM is generally associated with land cover change that can encompass large areas, including the clearing of primary tropical rainforest.

While the presence of this type of mining in small pockets of the Amazon Basin is not relatively new, the expansion of ASGM as a driver of land-cover change throughout Amazonia and in other tropical ecosystems has increased markedly over the past decade. For instance, in the Peruvian department of Madre de Dios, ASGM was responsible for the removal of over 120,000 ha of primary tropical forest from 1984 to 2017 [4]. ASGM has also taken hold outside the Amazon, including Nigeria [5], Ghana [6], Laos [7], and Indonesia [8]. The intensification of ASGM has led to profound impacts on river biogeochemistry [1], human health [9], and conserved areas [4], making it a significant driver of land-use change in tropical landscapes and riverine systems. Water is essential for the mining process, and shallow tropical water tables quickly fill any excavation. The result of this is that entire landscapes that were once primary forests have been converted to a mixture of ponds and bare earth, creating novel hydroscapes and greatly changing restoration potential [10] (**Figure 1**).

Figure 1: Mining ponds in La Pampa showing a range of activity levels. Deep green ponds indicate the presence of algae and the cessation of mining activity. Chalky clay-colored ponds contain high levels of suspended sediment and are currently actively mixed. Light green ponds, such as the one in the center of the image, are transitioning from active status to inactive status.

As ASGM has intensified globally, monitoring efforts to detect mining activity have been of significant interest for conservation and governance purposes. Current efforts to monitor ASGM landscapes, including the presence of mining ponds and water bodies left over from sediment extraction, generally make use of satellite-based remotely sensed imagery (e.g., [4,11]). This work often relies on indices that compare reflectance band data from these sensors to categorize the land surface into broad categories, a technique that is also used for monitoring small water bodies [12–14]. However, these methods generally work on a pixel-basis, and do not keep track of temporal change across time series.

Recently, developments in deep learning have led to increased capacity for monitoring land use change more discreetly, allowing for segmentation and labeling of individual features or objects within digital imagery. Among these methods are the use of both convolutional neural networks (CNN) and recurrent neural networks (RNN). A convolutional neural network (CNN) is a multilayer neural network which is inspired by the model of the primate visual system [15] and is utilized for learning features [16] and classification problems [17,18]. Specifically, CNN relies on two-dimensional spatial contexts within imagery data to generate edges and identify features. As a result, CNN-based deep learning is widely used for feature extraction uses such as semantic segmentation [19], landslide detection [20], object detection [21,22], and change detection [23]. Comparatively, RNNs have the capacity of re-applying past weights to layers in the neural network remembering the spatial features over time, thereby utilizing temporal contexts and functionality with time-series data. RNNs have been used for monitoring and estimating land-cover change [24,25] and crop identification [26,27]. When these two types of neural networks are combined into a singular network (ReCNN; [28]), time-series multispectral data can be analyzed in a way that detects features as well as changes in conditions of these features over time.

While it may appear that deep learning only provides a more detailed estimate of land-cover change when compared to conventional techniques, these new methods may be transformative in guiding policy formation and mitigation measures. For instance, in the context of ASGM, general methods using spectral indices alone describe the area of primary tropical forest biomass that has been converted [4,29] as well as the presence of new mining ponds [10]. These mining ponds, or lagoons, are 3-4 m deep water bodies produced as sediment is piled and processed into large tailing mounds, and excavated areas are filled with water via hoses and pumps to hasten the erosion and dissolution of the soil. When nearby mining abates, sediment concentrations in the pond water column decrease while phytoplankton and algae increase in still water [1;30]. Understanding such changes provides insight into the effectiveness of mining and conservation policy across a landscape [30]. Ultimately, deep learning methods that provide time series data on the reflectance of individual features on a landscape may thus provide great utility for land-use change science and analysis.

In this work, we show how deep learning can be used to more thoroughly evaluate object-oriented land cover change via satellite imagery. To do so, we utilize ReCNN, a combined form of CNN and RNN into a singular network [31], to detect and categorize the changes of mining ponds created by ASGM activities, and compare this with a semi-supervised model, support vector machines with smoothed total variation, SVM-STV. Specifically, we examine the outcomes from these models, as well as a number of labeling methods, to understand the applicability of these techniques to land-cover change associated with ASGM. We focus on mined areas in the Peruvian department of Madre de Dios, a global hotspot of ASGM activity. We then transfer our model to other international ASGM sites to showcase its utility. Our primary contributions are:

- The creation of an open source labeled dataset of water body change pertaining to ASGM that can be used for training and consistent evaluation of algorithm performance;
- An evaluation of labeling methods and approaches for use with supervised model construction;
- An assessment of supervised and semi-supervised methods in the context of detecting and characterizing mining ponds from ASGM activity;
- A test of the best-performing models at a selection of out-of-sample international ASGM sites to examine universal model utility.

2. Materials and Methods

2.1. ASGM Ponds Dataset and Change Characterization

Our main study region is located within the Peruvian department of Madre de Dios (MDD), a global hotspot of ASGM activity. We selected 16 distinct smaller region samples (~70 km^2 each) of interest within MDD to highlight locations that had experienced mining pond surface area increases as well as notable deforestation (Figure 2; Table 1 in Appendix). These regions were selected for two main reasons: firstly, the regions spanned a gradient of significant mining intensity, techniques, and policy enforcement over the last 15 years. Secondly, the regions were shaped so as to maximize the number of pixels undergoing change between bi-temporal images, thereby providing a more thorough test of our models. A total selection of sixteen regions allowed for a fully representative sample of sites with these two considerations in mind.

We acquired Sentinel-2 Top-of-Atmosphere reflectance data for these 16 regions via the Google Earth Engine platform. The Sentinel-2 satellite constellation [32] was developed for monitoring variability in land surface conditions at frequent revisit time (5 days at the equator) and consists of 13 multi-spectral channels ranging from ultra-blue to shortwave infrared with pixel resolutions between 10 and 60 meters GSD. Sentinel-2 data is widely used to assess land cover change in the context of surface water [33,34]. We selected data from two different years (2019 and 2021) with very low cloud coverage to showcase periods in which significant land-use change had occurred. We removed the influence of atmospheric effects by histogram matching of corresponding images of the same region and used Sentinel-2 metadata about cloud cover to remove any residual clouds on the images.

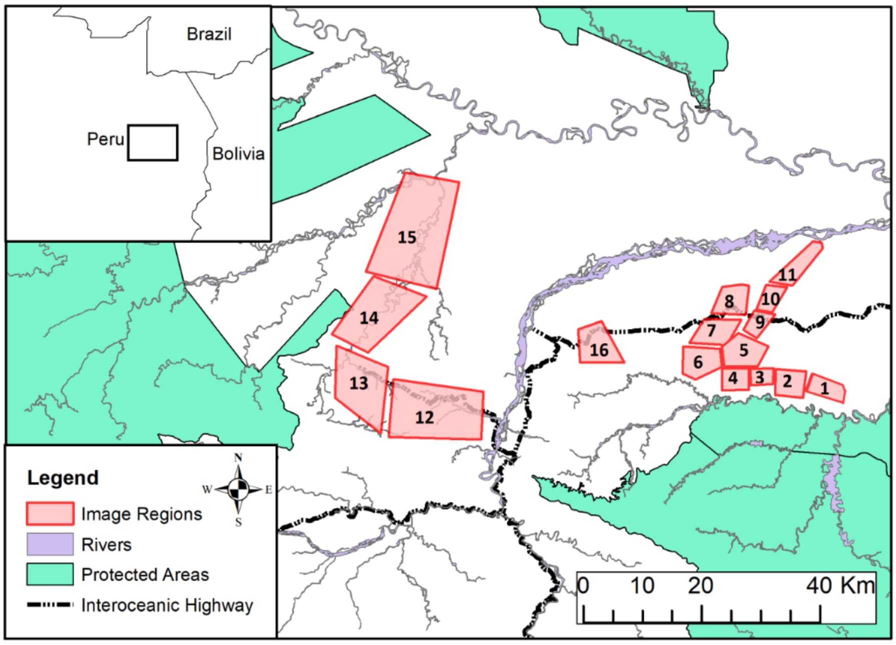

Figure 2. Selected sixteen region samples are shown with different transparent colors in the Madre de Dios (MDD) area on Google Earth Engine (GEE) seen on 07/23/2021. For more geographical details about each region sample, see Table1 and Figure1 in Appendix.

Land use changes due to alluvial gold mining occur across different parts of the world so it is crucial that change detection algorithms generalize from one geographical region to another. Thus, we included an out-of-sample testing dataset containing instances of similar alluvial gold mining in Indonesia, Myanmar, and Venezuela. (**Table 2 in Appendix**). Mining in these regions are of similar intensity to that in MDD.

For the purpose of generating meaningful labeled data, we defined three different pond states in relation to the recency of mining:

- **Active state**: where mining was ongoing at the time of image collection,
- **Transition state**: where mining was recent but not ongoing; and
- **Inactive state**: where mining had ceased longer than 6 months prior to imaging.

Change in mining ponds was then defined as follows:

- **Decrease:** change from active to inactive, active to transition, or transition to inactive;
- **Increase:** change from inactive to active, inactive to transition, or transition to active;
- **Water Existence/Absence:** change from water to no-water or no-water to water; and,
- **No Change:** no state changes between time periods took place.

These basic categories can provide useful information regarding ongoing mining activities, such as intensification, cessation, and the effect of governance [1,4].

A subgroup of individuals in our research group with expertise in the characterization of alluvial gold mining manually segmented and labeled each individual pond in our dataset. Ponds were segmented by manually tracing their edges and pond status was determined from side-by-side visual observation of the RGB and Shortwave-infrared (SW) with GB composite images for each region, see Figure 3 a, b, c). These band combinations were chosen specifically to help discriminate between active sites, in which sediment highly reflects in the red band, and inactive sites, in which photosynthetic material is present and influences the shortwave infrared reflectance (**Figure 3a**). For consistency, we calculated color index C_{idx} = (green - red)/(green + red) distributions of pond pixels and chose thresholds of 0 and 0.15 to select ponds in a transition state.

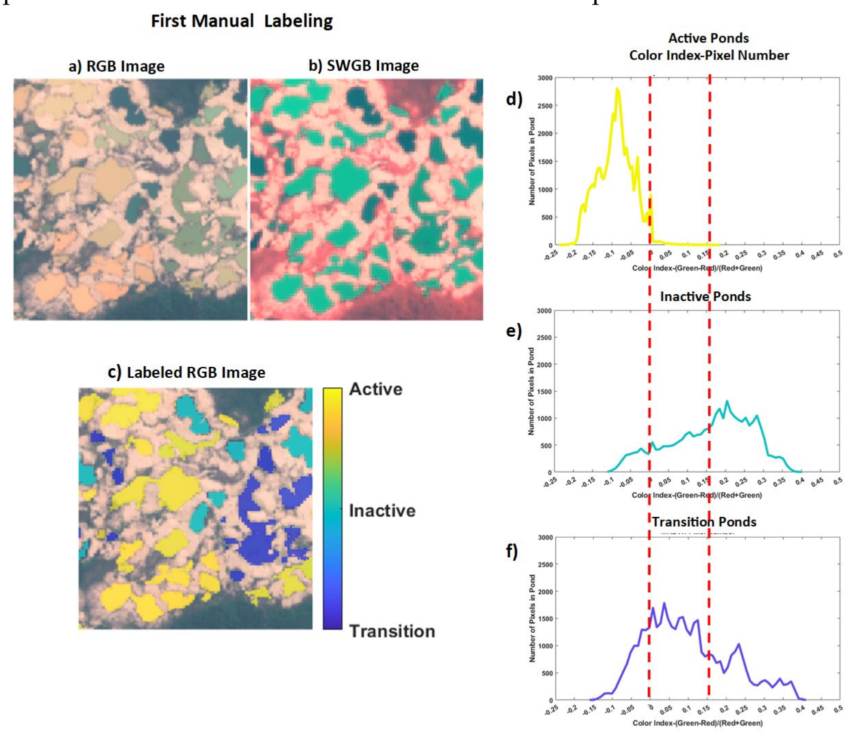

Figure 3. We manually labeled the state of each pond using the Labelbox tool using RGB and SWGB composite images. The composite images (**a**) RBG and (b) SWGB images display a multitude of ponds quite clearly, and label categories (**c**) affixed to these images. Using a color index [(green - red)/(red + green)], ponds can be differentiated with

respect to the presence of sediment and photosynthetic material and describe (**d**) active, (**e**) inactive, and (**f**) transition ponds.

2.2. Modeling Approaches

We considered two main approaches for modeling and quantifying change in residual ponds: a supervised deep learning method based on ReCNN [28] and a semi-supervised method involving a support vector machine and smoothed total variation regularizer [35].

2.2.1. Supervised Deep Learning Approach

We extended the ReCNN model of Mou et al. [28], originally designed to detect land cover type changes in urban areas using satellite imagery, for detection of large and subtle changes relative to water bodies. First, we augmented the ReCNN model to include a second LSTM plus dropout layer between the original two LSTM layers (**Figure 4**) to capture subtle pond state changes. Second, we modified the input layer to receive two temporal images separately, instead of two concatenated images as is done in other studies (e.g., [36,37]). We refer to this implementation as extended ReCNN (E-ReCNN) throughout the remainder of this paper.

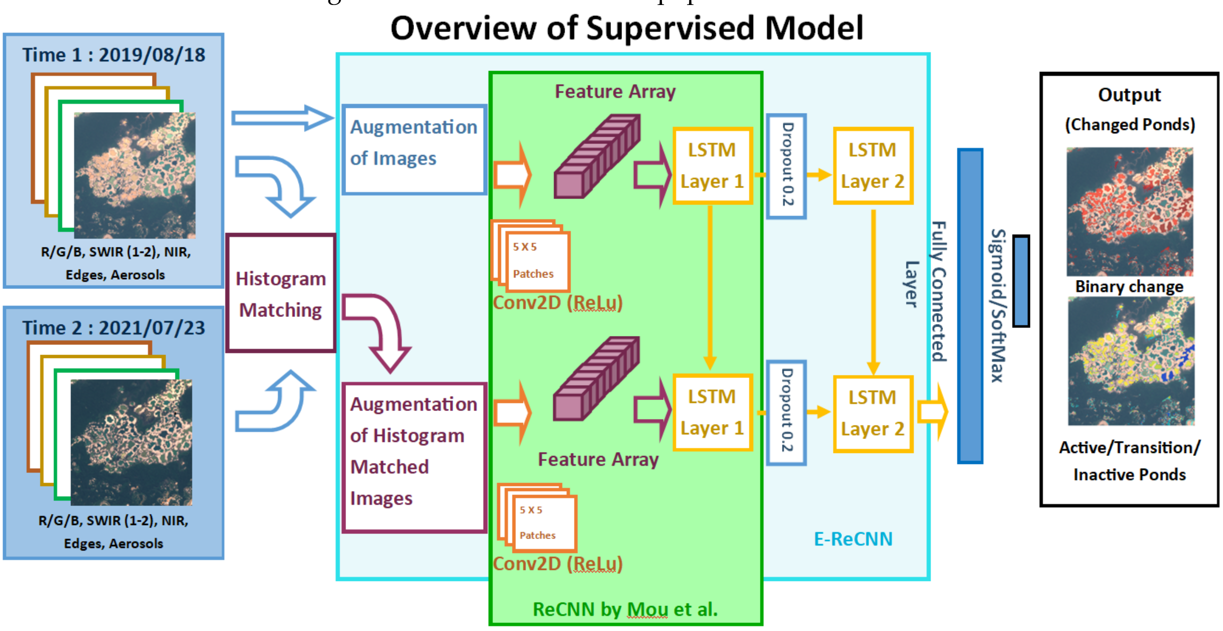

Figure 4. The E-ReCNN model uses two cloud-free Sentinel 2B images obtained from two different times (08/18/2019 and 07/23/2021) for the same region. Following histogram matching and augmentation, we used a convolutional kernel (Conv2d) on 5x5 pixel patches across each image to generate a feature array. These feature arrays then served as the input of the first LSTM layer and the second LSTM layer is formed following a dropout of 0.2. The last two layers were fully connected, and an output layer was applied with sigmoid/softmax functions to recognize the change of the pond's status.

2.2.2. Semi-supervised Deep Learning Approach

Unsupervised and semi-supervised learning methods are widely applied in remote sensing applications involving small datasets and limited access to high-performance computing equipment. SVMs are powerful semi-supervised approaches that have been used to detect land cover change utilizing spectral information of each pixel separately [38–40]. A recent approach SVM-STV by Chan et al. 2020 [35] also utilizes spatial information contained across image regions. We modified this approach to include a lifting option for multispectral images. Lifting is a preprocessing step that can help aid with segmentation of RGB images through the use of color spaces and additional features

[41–44]. We combined the RGB and La*b* color spaces in our images as features and then performed segmentation to reduce the effects of high correlation in one color space [44].

Figure 5 illustrates the two main steps in SVM-STV. In the first step, we form the v feature vectors from the difference in the bi-temporal images. Then we use a pixel-wise ν-Support Vector Classifier (ν-SVC) with a radial basis function kernel to find a hyperplane maximizing the margins between each pair of classes, using a one-against-one strategy, and to assign each pixel a vector of probabilities of belonging to each class [45,46]. The difference in La*b* color space between bi-temporal images is included in feature v if the lifting option is enabled. In the second step, a smoothed total variation (STV) regularizer smooths the probability vector and consequently the classification map.

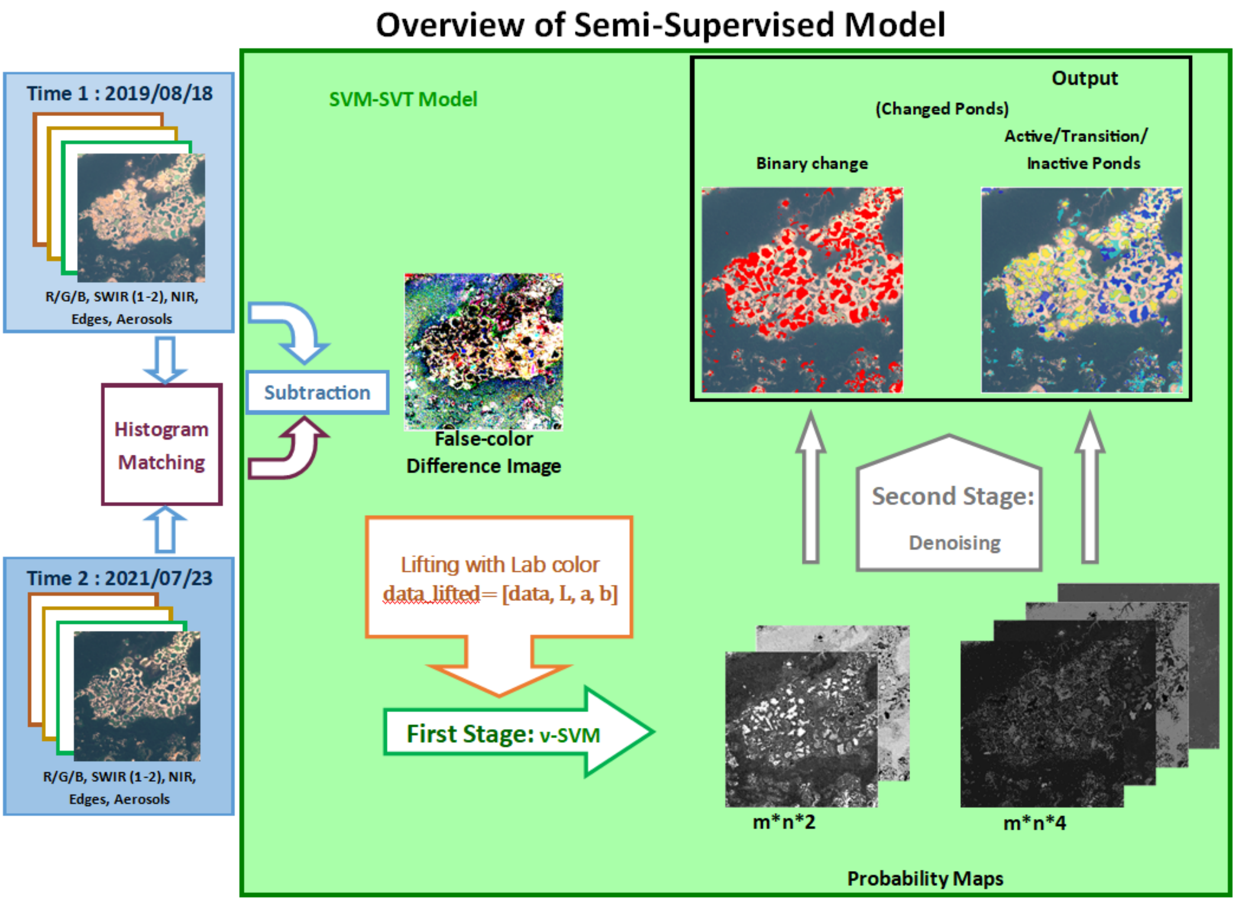

Figure 5. Overview of the SVM-STV method for mining change recognition. Bi-temporal images from a region are used as inputs. Preprocessing steps utilize histogram matching and lifting with Lab color data for both images. Labeled points using different images are used to train the ν-SVM in the first stage and then used to generate probability maps. In the second stage, spatial information is utilized by denoising the probability tensor. The final classification results are obtained by taking the index of the maximum probability of each pixel to detect change.

2.2.3. Statistical Approaches, Training, and Operation

In order to understand the performance of our proposed approaches, and the impact of spectral information and image pre-processing, we designed a number of test-train experiments across the 16 numbered regions within Madre de Dios (**Figure. 2**). Additionally, to examine the generalizability of our approaches to ASGM sites in other locations in the tropics, we constructed a set of out-of-sample testing regions in Venezuela, Indonesia, and Myanmar.

Since our supervised and semi-supervised modeling approaches used different quantities and distributions of labels, we used slightly different training approaches for each model. For the E-ReCNN model, we used a leave-one-region-out cross-validation approach. This method is often used for classification in medical imaging (e.g., leave-one-patient-out) [18,47] to account for class imbalance and region information. Specifically, we left one of the sixteen MDD regions out for testing and used the remaining fifteen regions for training and validation. We iterated this process for each individual region, allowing each region to serve as a testing region once. For each iteration, one region's image was selected as a test, and the remaining fifteen regions' images were used for training (70% of all patches) and validation (30% of all patches). Because we were examining the influence of the number of channels included in the model, this process was repeated for each multispectral image in the 3, 6, and 10-Channel image sets. Nesterov Adam [48], an improved Adam optimizer [49] was used to accelerate adaptive moment estimation and the convergence of both the Adam and stochastic gradient descent (SGD). The parameters of the model producing the best average predictive results are listed in Appendix Table A2. All testing and training using E-ReCNN were performed on the Wake Forest University DEAC HPC Cluster [50] (Appendix Table A3).

To train the SVM-STV semi-supervised model, we first trained the ν-SVC and then performed denoising on the probability map that ν-SVC produces. In the context of semi-supervised learning, less than 1% of labels were randomly selected for training whereas over 99% of the labels were unknown. Thus, in the training process of each region, instead of including all the pixels into the ν-SVC, we only incorporated a subset of randomly chosen labeled points from each region. So, for each of the 16 MDD regions, we first specified the number of labeled pixels per class (N_k) for training the model. Next, we used the preprocessed randomly selected $N_k * K$ labeled pixels to train the ν-SVC with five-fold cross-validation, where K is the number of classes. The trained ν-SVC was then applied to predict the probability tensor, and finally the denoising parameters were tuned based on the probability maps of each region. The training procedure for SVM-STV was computationally feasible and had a rapid training time as it only used a small portion of randomly selected labeled data (0.004% - 0.2%). All testing and training of the SVM-STV method were conducted in the same environment: Intel® Core™ i7-10875H CPU @ 2.30GHz, 8 cores, 64 GB RAM, Windows 64-bit system, and MATLAB R2021a.

To examine the influence of spectral information on method performance we constructed three sets of spectral images with varying numbers of spectral bands chosen specifically for application to water and land cover change:

- A three-band set of images containing red, green, and blue bands (RGB);
- A six-band set of images containing red, green, blue, NIR, SWIR1, and SWIR2;
- A 10-band set of images containing red, green, blue, NIR, SWIR-1, SWIR-2, ultra-blue, and bands 5, 6, and 7 which correspond to vegetation red edge.

To evaluate the overall performance of our methods, we used three metrics: the Cohen Kappa coefficient [51], the Jaccard index [52], and the F-1 score [53,54]. The Cohen Kappa coefficient provides a measure of consistency and reliability in classification tasks. The Jaccard index also referred to as the intersection over union, measures the overlap between labels and predictions, emphasizing true positives over true negatives. The F1 measure is the harmonic mean between precision and recall and does not take true negatives into account which ensures the changed area accuracy is not affected by 'no change' area accuracy which is high because of the number of pixels. We did not calculate accuracy scores, as these can be misleadingly high due to severe class imbalance.

3. Results

In this section, we present the results of multiclass change detection on AGM ponds in multispectral images which were obtained from focal (MDD) and out-of-sample prediction regions. Results from change detection analyses using binary classes (change/no change) can be found in Appendix Table A6 and A7.

The overall performance of our two approaches, across testing regions and using all testing sets with respect to the number of channels ranged from 0.19(±0.06) to 0.92(±0.04), with the inclusion of increased spectral information (channels) positively associated with increased performance. Among all experimental settings, the greatest average result of multiclass change classification by E-ReCNN was a Cohen Kappa of 0.92(±0.04), a Jaccard value of 0.88(±0.07), and an F1 of 0.88(±0.05) for histogram matched 6-Channel set images. In contrast, the greatest average result of a multiclass change by SVM-STV was a Cohen Kappa value of 0.63(±0.07), a Jaccard value of 0.56(±0.06), and an F1 of 0.67(±0.06) for original (not preprocessed) 10-Channel set images. These results were achieved on images from the MDD region training dataset. The MDD-trained E-ReCNN approach applied to out of sample regions (Figure 6, right) performed similarly to the results obtained in the focal MDD region (Figure 6, left) which shows the generalization of E-ReCNN across different spatial regions. The SVM-STV approach performed less-well on out-of-sample prediction, decreasing by 25% on average.

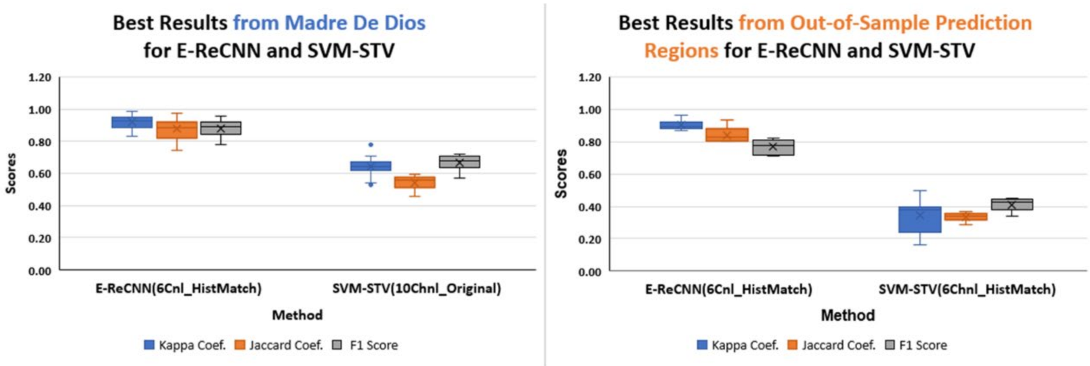

Figure 6. (left) Average scores of model performance across the 16 MDD regions for both E-ReCNN and SVM-STV. The highest accuracies were generated with the 6-channel set of histogram matched data for E-ReCNN and with the 10-channel data for SVM-STV. **(right)** Average scores of model performance for out-of-sample test regions in Indonesia, Myanmar, and Venezuela for both E-ReCNN and SVM-STV. The highest accuracies were generated with the 6-channel set of histogram matched data for E-ReCNN and with the 6-channel histogram matched data for SVM-STV. For both left and right, blue, orange, and gray boxes represent the distribution of Cohen Kappa coefficients, Jaccard coefficient, and F1 scores respectively.

Overall, E-ReCNN model performance using the 6-channel histogram matched image sets from the 16 MDD regions resulted in outcomes with high levels of precision, recall, and F1 score (Figure 7, left). Model F1 scores for ‘no change’ and ‘water existence’ classes were 0.99 and 0.96, respectively. F1 scores for ‘increase’ and ‘decrease’ classes of pond turbidity were slightly lower than ‘no change’ and ‘water existence’ classes, although the total quantity of labeled pixels for those two classes was notably lower. This pattern of F1 scores across classes was also seen in the out-of-sample regions (Figure 7, right). The total number of classified pixels in these regions was significantly lower, and F1 values for ‘decrease’ and ‘increase’ classes were 0.56 and 0.57 respectively. Performance metrics that are not biased by smaller sample sizes, including Cohen Kappa and Jaccard coefficients, were higher than 0.9 for both the MDD regions as well as international out-of-sample regions. In contrast, SVM-STV model results for ‘water existence’, ‘increase’, and ‘decrease’ classes were less accurate than E-ReCNN model results as shown in Figure 8 for the MDD regions (left) and out-of-sample regions (right). F1 scores for the MDD region ‘increase’ and ‘decrease’ classes were lower using this semi-supervised method than the out-of-sample regions as modeled by E-ReCNN. Model results for the out-of-sample regions using SVM-STV were very low with respect to F1 scores, below 0.15 for the 'increase' and 'decrease' classes.

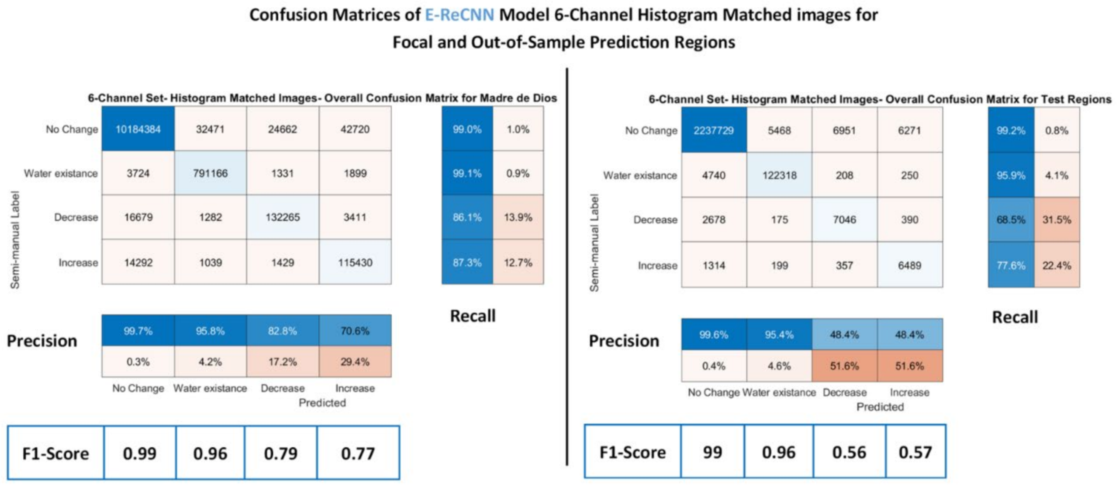

Figure 7. Confusion matrices for the E-ReCNN model for 6-Channel set histogram matched images from the MDD focal regions (**left**) and out-of-sample prediction regions (**right**). For both **left** and **right**, recall and precision matrices are featured to the right and below the main confusion matrix, respectively. Arrays at the bottom of both **left** and **right** show the F1-score for each class.

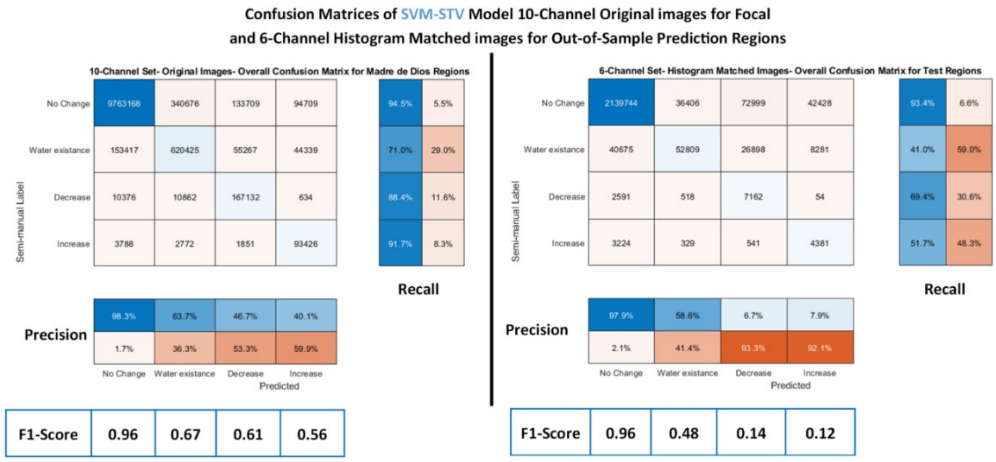

Figure 8. Confusion matrices for the SVM-STV model for 10-Channel image sets from the MDD focal regions (**left**) and 6-channel histogram matched images for the out-of-sample regions (**right**). For both **left** and **right**, recall and precision matrices are featured to the right and below the main confusion matrix, respectively. Arrays at the bottom of both **left** and **right** show the F1-score for each class.

Applying the E-ReCNN and SVM-STV models on image sets with a variety of spectral channels provided inference regarding how each channel of Sentinel-2 influenced model behavior. The 3-channel RGB image resulted in roughly equivalent F-1 scores for both the E-ReCNN model and the SVM-STV model across the MDD regions (Figure 9). While the addition of near-infrared and short-wave infrared channels (1&2), which are often used to define water surfaces with the help of a water index (6 channel image), improved F-1 scores for both models, further including red edge channels (10 channel image) resulted in no additional improvement. Notably, E-ReCNN results appeared to be more accurate than SVM-STV for both the 6-channel and 10-channel image sets.

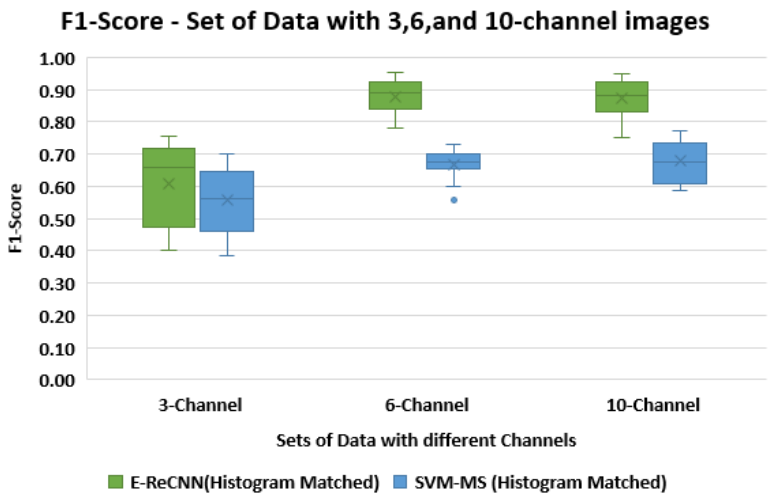

Figure 9. Analysis of multiclass results according to different numbers of channels by F1 score. Results of histogram matched images according to 3, 6, and 10-Channel sets are shown in F1-score based. The E-ReCNN model results are higher accuracy than the SVM-STV model results. The 6-Channel results average is more accurate and has less standard deviation than the 3 and 10-Channel results.

4. Discussion

In the context of land-use change, particularly change associated with ASGM, understanding how features across a landscape change in size and reflectance can provide critically important information for conservation and environmental policy enforcement. We show that our extension of an existing ReCNN detects multi-temporal change across landscape features when compared to an existing semi-supervised model (SVM-STV). E-ReCNN outperformed SVM-STV and unsupervised methods considerably for both our focal region in Madre de Dios, as well as out-of-sample test regions, with respect to F1, precision, and recall. Notably, E-ReCNN generated greater F1, precision, and recall values for the detection of water occurrence and the multi-temporal change in spectral response for each pond feature. Estimates of precision and recall for pond sediment decrease (82.8% and 86.1%) and increase (70.6% and 87.3%) within MDD show that this method is capable of generating multi-temporal feature-based change maps, providing evidence that this method has wide applicability to the field of environmental change detection and monitoring.

One ongoing challenge in the use of satellite data for change detection relates to how atmospheric conditions can cause complications when attempting to document fine-scale feature-oriented change. Although the major remotely sensed platforms such as Landsat, Sentinel, and MODIS are routinely processed and corrected via well-established and formalized techniques [55–58], variability in surface reflectance from image to image requires careful consideration for the establishment of defined trends. In our analysis, we tested a number of data pre-processing approaches to understand how these challenges could be addressed and to understand how steps can be taken to improve machine learning model results. We found that histogram-matching, which has primarily been used in remote sensing to denoise atmospheric effects on image mosaics [59,60], and recently in change detection [61–63], improved outcomes for our supervised model, E-ReCNN. In contrast, including Lab color space variables into the semi-supervised model, SVM-STV, produced the most accurate results. While water surface change detection datasets using remotely sensed imagery indicate excellent results without histogram-matching (e.g., [64–66]), we note that these studies focus on large-scale changes in deep surface water extent/presence, wherein atmospheric noise plays less of a factor. In our case, where we attempt to identify more subtle changes in water reflectance, we find that these preprocessing steps are necessary to achieve optimal results in detecting changes in water bodies resulting from ASGM and should be considered in land-use change detection workflows, particularly if top-of-the-atmosphere products are utilized.

In addition to pre-processing methods, decisions regarding the inclusion of specific channels of remotely sensed data into models for analyzing land cover change dynamics are important to ensure accurate outcomes. Critical tradeoffs between sensor spatial resolution, temporal resolution, and the availability of spectral channels can constrain the scope of land-cover change analysis. In the context of ASGM mining pond detection and classification, where patterns across years and seasons are evident, newly established commercially available satellite imagery (PlanetScope, DigitalGlobe) provide the temporal and spatial resolution necessary to detect these fine-scale changes; however, these products generally are only available in a narrow set of channels. In our results, we found that the supervised E-ReCNN model generated the best outcomes in the 6-Channel and 10-Channel data sets after histogram matching, with significantly lower F1 scores in the 3-Channel data set. When we applied lifting using L*a*b color space variables, the results either did not impact (for the 10-channel data set) or slightly decreased (for the 3- and 6-channel data sets) accuracies. Consequently, we conclude that the selection of RGB images for this type of change detection may result in inferior outcomes compared to data sets with a greater number of channels in the infrared and red-edge spectrum. Commercial satellite data that lack these channels may be therefore limited in detecting important changes in aquatic systems, at least in comparison to other options.

Our modeling results show a notable difference in accuracy between supervised and semi-supervised methods. Although novel unsupervised learning methods presented in the literature show a great deal of potential for change detection [67–69], when we utilized one such unsupervised learning method [70], model performance results were substantially weaker than those provided by E-ReCNN and SVM-STV. Thus, we did not include detailed results regarding using unsupervised learning techniques for this problem. Our semi-supervised method, SVM-STV, in general fits the data effectively by making use of a small fraction of labels, especially when only RGB data is provided. Our results indicate that if a small, labeled set of a mining region in MDD is retrieved, the SVM-STV method can be trained on a desktop computer in a matter of minutes and produce reasonable results for both binary and multiclass classification. In practice, users can decide the number of expert-generated labels to acquire based on their needs, with the caveat that a fully supervised model may be more accurate and precise. In addition, if RGB images are necessary for detecting rapid change at localized scales, lifting using the La*b* color space generates enhanced results compared to data that has not been pre-processed.

Supervised model performance varied across MDD training regions (Appendix Table A4) with respect to temporal change, but was consistent across regions for detecting change/no change, with change detection F1 scores higher in regions using water cannons compared to regions using earth moving equipment. For example, region 4 within La Pampa is characterized by ovular ponds with distinct edges surrounded by bare ground (Figure 10, top). This region has been heavily mined using suction pumps to displace water into mining ponds and use small sluices to separate fine sediment from larger stones and pebbles. Comparatively, region 12 in Huepetuhe (Figure 10, bottom) features the signature of the use of bulldozers and excavators to move sediment for processing; consequently, this region lacks distinct ponds with clear edges as in region 4. We suspect that the lack of defined edges of water bodies provided an additional challenge for convolutional filters within E-ReCNN, leading to a decrease in the F1 score in the region 12. Our results indicate that regions where mechanized mining is more prevalent are modeled with lower values for detecting increases and decreases in pond reflectance than those regions in La Pampa and, subsequently, monitoring and modeling directional pond change may be more difficult in areas with differing mining typologies;

however, outcomes for detecting change/no-change and water existence were excellent for both methods (Appendix Table A6 and A7).

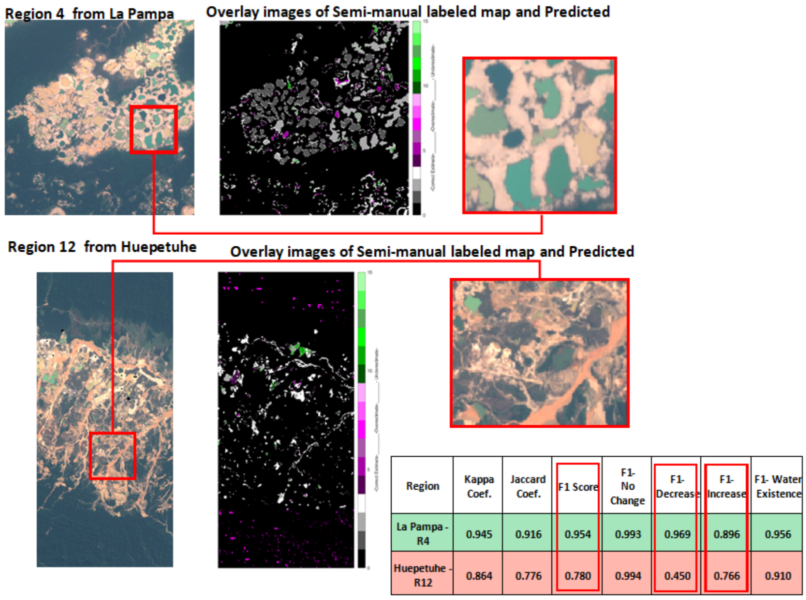

Region	Kappa Coef.	Jaccard Coef.	F1 Score	F1- No Change	F1- Decrease	F1- Increase	F1- Water Existence
La Pampa - R4	0.945	0.916	0.954	0.993	0.969	0.896	0.956
Huepetuhe - R12	0.864	0.776	0.780	0.994	0.450	0.766	0.910

Figure 10. True-color image composites of region 4 in La Pampa (**top, left**) and region 12 in Huepetuhe (**bottom, left**) show how signatures of mining using different practices may generate more or less uniform surface water bodies. The middle images are overlay images of semi-manual label maps and model-predicted results, with white and shades of gray representing accurate classification, shades of magenta representing overestimated sediment, shades of green representing underestimated sediment, and black representing no detected change. While Region 4 from La Pampa has deeper and more circular ponds that are separated from sand, Region 12 from Huepetuhe has more shallow, small and intricate ponds mixed with sand and ground, which appears to impact accuracy metrics.

Whereas model outcomes were generally accurate across MDD regions, with slight differences between areas with different mining types, model results in the out-of-sample international regions were slightly less accurate with respect to multi-class change detection. However, with E-ReCNN, our out-of-sample results were still within 10% of our focal region results, indicating that this method retained significant performance of detecting change/no change and water occurrence in ASGM sites in different contexts and on different continents. With respect to pond increases and decreases in turbidity, both supervised and semi-supervised models generated significantly lower recall and precision for international sites compared to the MDD region results. Semi-supervised results using SVM-STV were extremely inaccurate (Figure 8, right) indicating that using this method is not advisable for accurate change detection; supervised model results were less accurate for these out-of-sample regions, but still detected binary classes of change quite accurately overall. The construction of regional label sets may improve performance for detailed questions regarding pond status, but for general detection of AGM associated mining ponds, the supervised model appears suitable for inference world-wide. More thorough investigations at known mined sites across the tropics would provide greater detail regarding the variability of model performance in new regions.

5. Conclusions and Future Work

In this paper, we describe the creation of a unique ASGM Residual Ponds dataset as well as a new supervised method (E-ReCNN) for detecting fine-scale changes in the environment using satellite imagery. We show how this method compares favorably to existing semi-supervised (SVM-STV) methods. We applied different preprocessing operations on three image sets with different quantities of multispectral bands to analyze their influence on the models' results. According to our analyses with Sentinel-2 imagery, using a 6-band image set generated model performance higher than other band combinations, even those that included more spectral information. Pre-processing was essential to model performance, even on well-curated Sentinel-2 data, increasing model F1 scores from roughly 0.71 to 0.88 for 6-band images. For fine-level change detection we conclude that these images need noise reduction and calibration such as histogram matching for E-ReCNN and the addition of La*b* color space to the SVM-STV model. Given this finding, practitioners using other change-detection methods on available satellite imagery, particularly with respect to water detection, may benefit from revisiting their results and investigating whether inaccuracies were due to pre-processing impacts.

Practitioners wishing to use the methods presented in this manuscript should consider the practical and computational demands of both change detection models. We found that classification performance is inverse to the computation demands for the two methods. Since the SVM-STV model can be trained on local machines, it is an efficient solution under the conditions of limited channels and resources. In contrast, because the E-ReCNN model consists of CNN and LSTM subnetworks, the R-ReCNN model requires considerably lengthy training times on GPUs (Appendix Table 3). However, it is worth noting that the E-ReCNN model, once trained once, appears to be capable of extension to out-of-sample regions with minimal loss in performance, and therefore once this process is completed, this method can be applied globally.

Future work may allow for an improvement of the SVM-STV model, particularly since the training size of labeled pixels used in this test was small and likely contained outliers and noisy pixels that could affect the quality of the model. Although histogram matching reduces radiometric differences in bitemporal images, the disparities among training regions can be significant and influential. Instead of randomly selecting training pixels for a generalized model, kernel density estimation may be used as an indicator that gives information of the "commonness" of each pixel [70,71]. This allows for the exclusion of outliers by only selecting pixels at high densities, generating more consistent test results. Furthermore, the SVM-STV model may be improved by including an active learning scheme, which takes into account the practical condition that there is a restricted budget for label collection. The diffusion geometry of the data can be used to push the approach even further by reducing the number of labels needed but producing greater performance [70–72].

Follow-up work on E-ReCNN may allow for the application of this model to other landscapes and environmental topics. While we investigated bi-temporal imagery sets in this analysis, the performance of E-ReCNN across a multitemporal image set may offer information regarding model transferability for decadal estimates of change across a landscape. Furthermore, testing E-ReCNN for use with other environmental features for the detection of change such as fields, roads, and vegetation patches may allow for broad expansion of this supervised method to help monitor environmental change in other contexts and locations.

Supplementary Materials: We will share the GitHub repository.

Author Contributions: Conceptualization, V.P.P., D.L., M.S., L.E.F., and S.A.; methodology, V.P.P, S.A., R.C., S.C., and K.C.; software, S.C., K.C.; validation, V.P.P., D.L., M.S., S.A., S.C., and K.C.; formal analysis, S.C., K.C.; investigation, S.C., K.C.; resources, S.C., E.N.D.; data curation, S.C..; writing—original draft preparation, S.C., K.C., and D.L.; writing—review and editing, V.P.P., D.L., M.S., S.A., R.C., L.E.F., E.N.D., and R. J. P.; visualization, S.C.; project administration, D.L.; funding acquisition, D.L., All authors have read and agreed to the published version of the manuscript.

Funding: This research was funded by NASA award 20-LCLUC2020-0025, USAID Cooperative Agreement #72052721CA00005, a Neukom Postdoctoral Fellowship to E.N.D. Also support from USAID Cooperative Agreement #72052721CA00005.

Data Availability Statement: Zenedo or our web page

Acknowledgments: Computations were performed using the Wake Forest University (WFU) High Performance Computing Facility, a centrally managed computational resource available to WFU researchers including faculty, staff, students, and collaborators.

Conflicts of Interest: The authors declare no conflict of interest.

Appendix A

Table A1. The regions in Figure 2 with their sizes in pixel and in km2 area and their latitude and longitude of left bottom and right top.

Region Number	Size in Pixels	Area in Km2	Left bottom	Right Top
Region-1	667 x 654	43.37	13°01'51.9"S 69°55'29.5"W	12°58'15.9"S 69°51'53.5"W
Region-2	667 x 655	43.37	13°01'21.8"S 69°58'37.3"W	12°57'45.8"S 69°55'01.3"W
Region-3	556 x 546	30.12	13°00'27.3"S 70°00'54.0"W	12°57'27.3"N 69°57'54.0"W
Region-4	556 x 545	30.12	13°00'43.6"S 70°03'19.6"W	12°57'43.6"S 70°00'19.6"W
Region-5	1109 x 548	60.25	12°59'42.4"S 70°02'36.0"W	12°53'42.4"S 69°59'36.0"W
Region-6	667 x 655	43.38	12°59'22.4"S 70°06'47.8"W	12°55'46.4"S 70°03'11.8"W
Region-7	888 x 482	42.42	12°57'16.3"S 70°04'57.0"W	12°52'28.3"S 70°02'18.6"W
Region-8	556 x 545	30.13	12°53'31.7"S 70°03'35.8"W	12°50'31.7"S 70°00'35.8"W
Region-9	556 x 546	30.13	12°55'34.6"S 70°01'14.7"W	12°52'34.6"S 69°58'14.7"W
Region-10	555 x 438	24.1	12°53'19.3"S 69°59'47.2"W	12°50'19.3"S 69°57'23.2"W
Region-11	1109 x 657	86.72	12°51'48.2"S 69°57'52.1"W	12°45'48.2"S 69°54'16.1"W
Region-12	1333 x 659	86.12	13°05'46.4"S 70°31'00.8"W	12°58'34.4"S 70°27'24.8"W
Region-13	894 x 1309	115.66	13°02'14.2"S 70°39'33.2"W	12°57'26.2"S 70°32'21.2"W
Region-14	1337 x 1311	173.56	12°56'48.5"S 70°38'10.1"W	12°49'36.5"S 70°30'58.1"W
Region-15	1560 x 1748	270.11	12°49'54.8"S 70°35'44.9"W	12°41'30.8"S 70°26'08.9"W
Region-16	668 x 655	43.38	12°57'55.2"S 70°16'12.7"W	12°54'19.2"S 70°12'36.7"W

Table A2. Configuration of optimal model parameters for supervised (E-ReCNN) and semi-supervised (SVM-STV) models.

E-ReCNN (TensorFlow Framework)	Nesterov Adam – β_1=0.9, β_2=0.999, ϵ=1e-07 Learning rate - 1e-03 Glorot uniform initializer – uniform distribution
SVM-STV	The two parameters of ν-SVC: Nu: 0-0.2, Gamma: 1/(n+2)-1/(n-2), where n is the number of bands. The denoising parameters: Alpha1: 0-1, Alpha2: [0, 0.5, 1, 2], Mu: 5. The above five parameters are tuned on each of the 16 training regions.

Table A3. Calculated costs of model training.

E-ReCNN (Wake Forest University DEAC HPC cluster)	Number of Epoch: 75	Total Loss: 0.0208	Time per epoch: 548s
SVM-STV (Local machine)	Number of Trials: 10	Training Error: Controlled by Nu	Time per trial: 3s to 94s

Table A4. Accuracies of regions and their areas for the E-ReCNN model for histogram matched 6-Channel images

Area	Number of the regions	Kappa Coef.	Jaccard Co-ef.	F1 Score	No Change	Decrease	Increase	Water Existence
La Pampa	1	0.932	0.889	0.941	0.995	0.938	0.865	0.965
	2	0.880	0.814	0.893	0.990	0.911	0.726	0.945
	3	0.891	0.826	0.918	0.988	0.923	0.813	0.948
	4	**0.945**	**0.916**	**0.954**	**0.993**	**0.969**	**0.896**	**0.956**
	5	0.913	0.863	0.923	0.988	0.924	0.819	0.964
	6	0.879	0.807	0.868	0.989	0.852	0.660	0.969
	7	0.951	0.921	0.887	0.993	0.884	0.685	0.985
	8	0.984	0.974	0.904	0.998	0.774	0.854	0.991
	9	0.924	0.875	0.914	0.993	0.869	0.847	0.950
	10	0.983	0.973	0.930	0.997	0.805	0.927	0.990
	11	0.977	0.961	0.799	0.998	0.460	0.752	0.988
Huepetuhe	**12**	**0.864**	**0.776**	**0.780**	**0.994**	**0.450**	**0.766**	**0.910**
	13	0.951	0.917	0.848	0.997	0.659	0.754	0.983
Delta	14	0.924	0.884	0.855	0.995	0.686	0.772	0.970
	15	0.930	0.889	0.839	0.992	0.636	0.740	0.987
Inambari Tributary	16	0.832	0.740	0.795	0.994	0.547	0.786	0.854

Table A5. The regions in the different parts of the world with their sizes in pixel and in km2 area and their latitude and longitude of left bottom and right top.

Region Number	Time1	Time2	Size in Pixels	Area in Km2	Left bottom	Right Top
Indonesia-1	8/20/2018	4/7/2019	666x667	44.51	0°44'39.4"N 110°42'25.3"E	0°48'15.4"N 110°46'01.3"E
Myanmar-2	12/3/2018	3/20/2021	664x668	43.54	11°56'19.2"N 99°16'20.4"E	11°59'55.2"N 99°19'56.4"E
Venezuela-3	12/10/2018	9/20/2020	666x667	44.25	6°11'42.9"N 61°33'15.9"W	6°15'18.9"N 61°29'39.9"W

Venezuela-4	12/10/2018	9/20/2020	666x667	44.25	6°08'07.3"N 61°29'46.0"W	6°11'43.3"N 61°26'10.0"W
Venezuela-5	12/10/2018	9/20/2020	556x556	30.73	6°10'19.6"N 61°29'24.8"W	6°13'19.6"N 61°26'24.8"W
Venezuela-6	12/10/2018	9/20/2020	887x490	43.27	6°08'47.2"N 61°31'18.5"W	6°13'35.2"N 61°28'40.1"W
Venezuela-7	12/10/2018	9/20/2020	666x667	44.25	6°10'07.4"N 61°27'48.5"W	6°13'43.4"N 61°24'12.5"W

Table A6. Binary Change detection results for the E-ReCNN method

			Kappa Coef.	Jaccard Coef.	F1 Score
Original Images	3 Channel	Average	0.63	0.52	0.81
		Std Dev	0.13	0.12	0.07
	6 Channel	Average	0.71	0.63	0.84
		Std Dev	0.23	0.21	0.16
	10 Channel	Average	0.70	0.62	0.83
		Std Dev	0.25	0.23	0.17
Histogram Matched Images	3 Channel	Average	0.53	0.42	0.76
		Std Dev	0.11	0.11	0.06
	6 Channel	Average	**0.92**	**0.87**	**0.96**
		Std Dev	0.04	0.07	0.02
	10 Channel	Average	0.92	0.87	0.96
		Std Dev	0.04	0.07	0.02
Histogram Matched + Lab Lifted Images	3 Channel	Average	0.45	0.37	0.71
		Std Dev	0.16	0.14	0.10
	6 Channel	Average	0.92	0.87	0.96
		Std Dev	0.04	0.07	0.02
	10 Channel	Average	0.91	0.86	0.96
		Std Dev	0.04	0.07	0.02

Table A7. Binary Change detection results for the SVM-STV method

			Kappa Coef.	Jaccard Coef.	F1 Score
Original Images	3 Channel	Average	0.44	0.60	0.72
		Std Dev	0.10	0.06	0.06
	6 Channel	Average	0.62	0.71	0.81
		Std Dev	0.08	0.05	0.04
	10 Channel	Average	0.67	0.74	0.84
		Std Dev	0.07	0.04	0.03
Histogram Matched Images	3 Channel	Average	0.52	0.65	0.76
		Std Dev	0.09	0.06	0.05
	6 Channel	Average	0.64	0.72	0.82
		Std Dev	0.07	0.04	0.03
	10 Channel	Average	0.62	0.71	0.81
		Std Dev	0.09	0.05	0.05
Histogram Matched + Lab Lifted Images	3 Channel	Average	0.61	0.71	0.80
		Std Dev	0.07	0.04	0.04

		Average	0.64	0.72	0.82
	6 Channel	Std Dev	0.08	0.04	0.04
		Average	0.62	0.71	0.81
	10 Channel	Std Dev	0.08	0.04	0.04

Appendix B

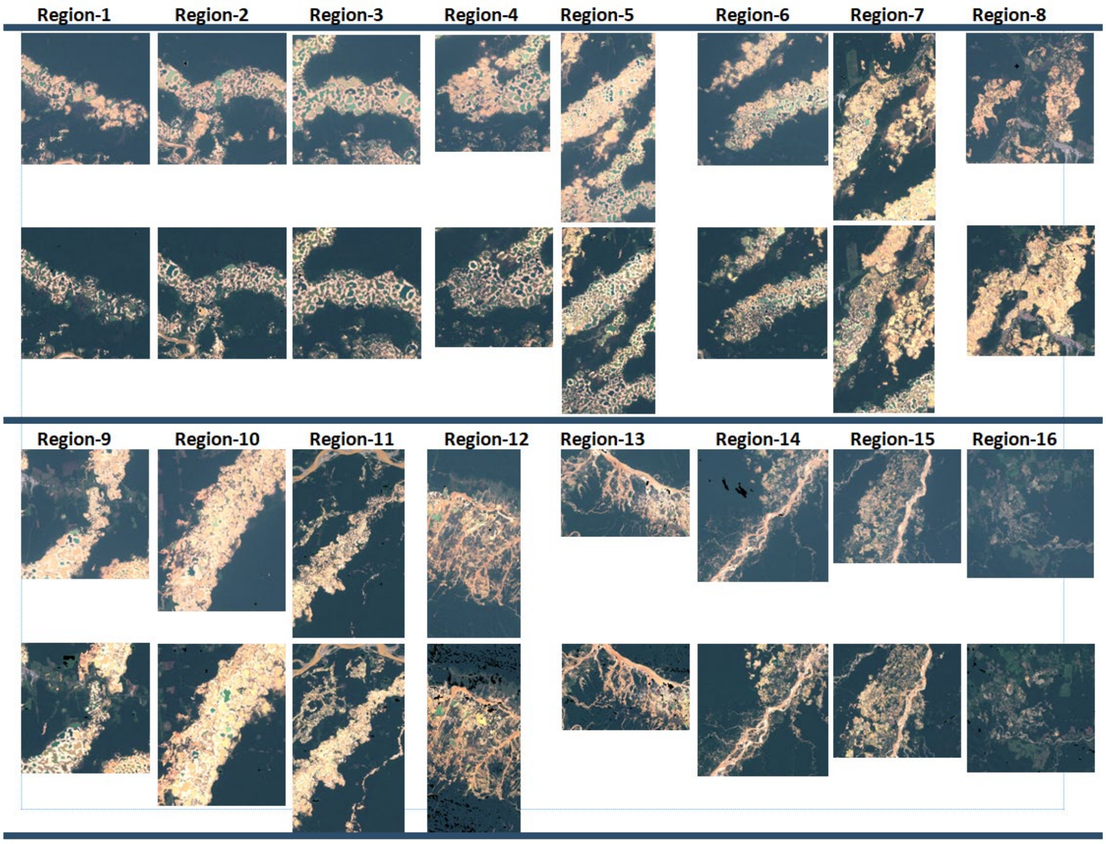

Figure B1. All images in MDD were used for LoRo experiments.

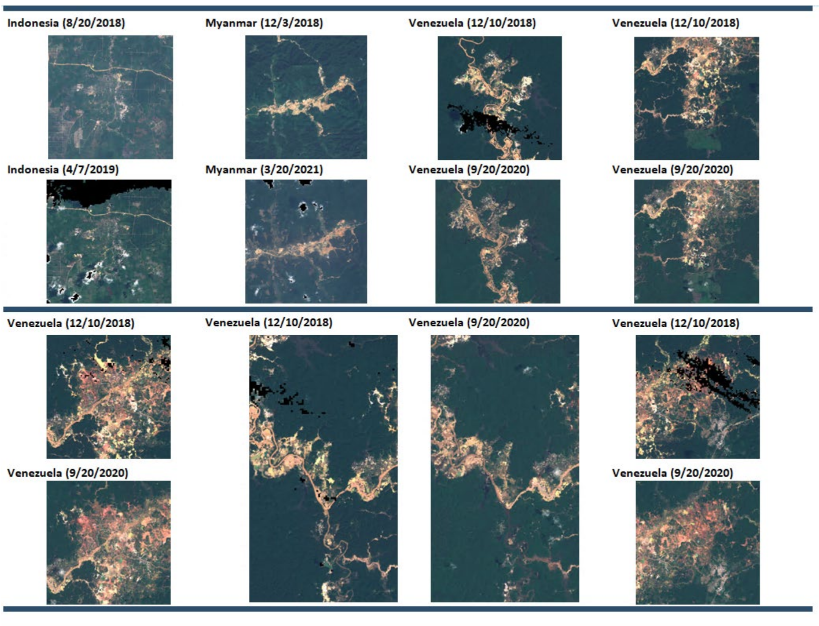

Figure B2. All Test images from Indonesia, Myanmar, and Venezuela.

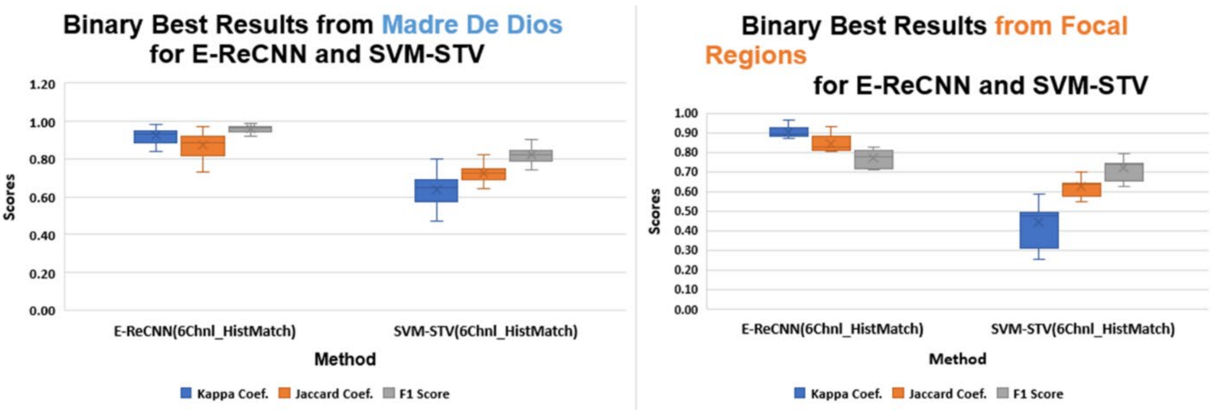

Figure B3. Binary change detection best performance.

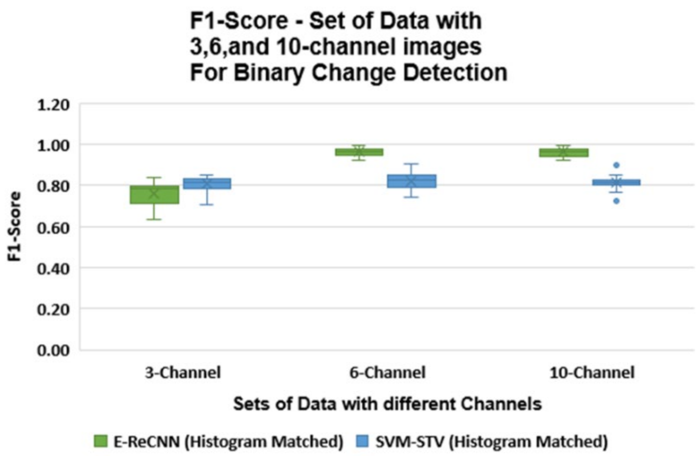

Figure B4. Binary Change Detection F1-Score for different channels.

References

1. Dethier, E. N.; Sartain, S. L.; Lutz, D. A. Heightened Levels and Seasonal Inversion of Riverine Suspended Sediment in a Tropical Biodiversity Hot Spot Due to Artisanal Gold Mining. *Proceedings of the National Academy of Sciences* **2019**, *116* (48), 23936–23941. https://doi.org/10.1073/pnas.1907842116.
2. Alvarez-Berrios, N. L.; Mitchell Aide, T. Global Demand for Gold Is Another Threat for Tropical Forests. *Environmental Research Letters* **2015**, *10* (1). https://doi.org/10.1088/1748-9326/10/1/014006.
3. Kahhat, R.; Parodi, E.; Larrea-Gallegos, G.; Mesta, C.; Vázquez-Rowe, I. Environmental Impacts of the Life Cycle of Alluvial Gold Mining in the Peruvian Amazon Rainforest. *Science of the Total Environment* **2019**, *662*. https://doi.org/10.1016/j.scitotenv.2019.01.246.
4. Caballero Espejo, J.; Messinger, M.; Román-Dañobeytia, F.; Ascorra, C.; Fernandez, L. E.; Silman, M. Deforestation and Forest Degradation Due to Gold Mining in the Peruvian Amazon: A 34-Year Perspective. *Remote Sensing* **2018**, *10* (12). https://doi.org/10.3390/rs10121903.
5. Taiwo, A. M.; Awomeso, J. A. Assessment of Trace Metal Concentration and Health Risk of Artisanal Gold Mining Activities in Ijeshaland, Osun State Nigeria— Part 1. *Journal of Geochemical Exploration* **2017**, *177*. https://doi.org/10.1016/j.gexplo.2017.01.009.

6. Owusu-Nimo, F.; Mantey, J.; Nyarko, K. B.; Appiah-Effah, E.; Aubynn, A. Spatial Distribution Patterns of Illegal Artisanal Small Scale Gold Mining (Galamsey) Operations in Ghana: A Focus on the Western Region. *Heliyon* **2018**, *4* (2). https://doi.org/10.1016/j.heliyon.2018.e00534.
7. Bounliyong, P.; Itaya, T.; Arribas, A.; Watanabe, Y.; Wong, H.; Echigo, T. K–Ar Geochronology of Orogenic Gold Mineralization in the Vangtat Gold Belt, Southeastern Laos: Effect of Excess Argon in Hydrothermal Quartz. *Resource Geology* **2021**, *71* (2). https://doi.org/10.1111/rge.12258.
8. Kimijima, S.; Sakakibara, M.; Nagai, M. Detection of Artisanal and Small-Scale Gold Mining Activities and Their Transformation Using Earth Observation, Nighttime Light, and Precipitation Data. *International Journal of Environmental Research and Public Health* **2021**, *18* (20). https://doi.org/10.3390/ijerph182010954.
9. Gonzalez, D. J. X.; Arain, A.; Fernandez, L. E. Mercury Exposure, Risk Factors, and Perceptions among Women of Childbearing Age in an Artisanal Gold Mining Region of the Peruvian Amazon. *Environmental Research* **2019**, *179*, 108786. https://doi.org/10.1016/j.envres.2019.108786.
10. Gerson, J. R.; Topp, S. N.; Vega, C. M.; Gardner, J. R.; Yang, X.; Fernandez, L. E.; Bernhardt, E. S.; Pavelsky, T. M. Artificial Lake Expansion Amplifies Mercury Pollution from Gold Mining. *Science Advances* **2020**, *6* (48). https://doi.org/10.1126/sciadv.abd4953.
11. Swenson, J. J.; Carter, C. E.; Domec, J.-C.; Delgado, C. I. Gold Mining in the Peruvian Amazon: Global Prices, Deforestation, and Mercury Imports. *PLoS ONE* **2011**, *6* (4), e18875. https://doi.org/10.1371/journal.pone.0018875.
12. Cooley, S.; Smith, L.; Stepan, L.; Mascaro, J. Tracking Dynamic Northern Surface Water Changes with High-Frequency Planet CubeSat Imagery. *Remote Sensing* **2017**, *9* (12), 1306. https://doi.org/10.3390/rs9121306.
13. Zou, Z.; Dong, J.; Menarguez, M. A.; Xiao, X.; Qin, Y.; Doughty, R. B.; Hooker, K. v.; David Hambright, K. Continued Decrease of Open Surface Water Body Area in Oklahoma during 1984–2015. *Science of The Total Environment* **2017**, *595*, 451–460. https://doi.org/10.1016/j.scitotenv.2017.03.259.
14. Wang, C.; Jia, M.; Chen, N.; Wang, W. Long-Term Surface Water Dynamics Analysis Based on Landsat Imagery and the Google Earth Engine Platform: A Case Study in the Middle Yangtze River Basin. *Remote Sensing* **2018**, *10* (10), 1635. https://doi.org/10.3390/rs10101635.
15. Kruger, N.; Janssen, P.; Kalkan, S.; Lappe, M.; Leonardis, A.; Piater, J.; Rodriguez-Sanchez, A. J.; Wiskott, L. Deep Hierarchies in the Primate Visual Cortex: What Can We Learn for Computer Vision? *IEEE Transactions on Pattern Analysis and Machine Intelligence* **2013**, *35* (8), 1847–1871. https://doi.org/10.1109/TPAMI.2012.272.
16. Camalan Seda AND Niazi, M. K. K. A. N. D. M. A. C. A. N. D. T. T. A. N. D. E. G. A. N. D. E. C. A. N. D. T.-S. N. A. N. D. G. M. N. OtoMatch: Content-Based Eardrum Image Retrieval Using Deep Learning. *PLOS ONE* **2020**, *15* (5), 1–16. https://doi.org/10.1371/journal.pone.0232776.
17. Morchhale, S.; Pauca, V. P.; Plemmons, R. J.; Torgersen, T. C. Classification of Pixel-Level Fused Hyperspectral and Lidar Data Using Deep Convolutional Neural Networks. In *2016 8th Workshop on Hyperspectral Image and Signal Processing: Evolution in Remote Sensing (WHISPERS)*; 2016; pp 1–5. https://doi.org/10.1109/WHISPERS.2016.8071715.
18. Camalan, S.; Mahmood, H.; Binol, H.; Araújo, A. L. D.; Santos-Silva, A. R.; Vargas, P. A.; Lopes, M. A.; Ali, K. S.; Gurcan, M. N. Convolutional Neural Network-Based Clinical Predictors of Oral Dysplasia: Class Activation Map Analysis of Deep Learning Results. *Cancers* **2021**, *13* (6). https://doi.org/10.3390/cancers13061291.
19. Yuan, X.; Shi, J.; Gu, L. A Review of Deep Learning Methods for Semantic Segmentation of Remote Sensing Imagery. *Expert Systems with Applications* **2021**, *169*, 114417. https://doi.org/https://doi.org/10.1016/j.eswa.2020.114417.

20. Mohan, A.; Singh, A. K.; Kumar, B.; Dwivedi, R. Review on Remote Sensing Methods for Landslide Detection Using Machine and Deep Learning. *Transactions on Emerging Telecommunications Technologies* **2021**, *32* (7), e3998. https://doi.org/https://doi.org/10.1002/ett.3998.
21. Hoeser, T.; Kuenzer, C. Object Detection and Image Segmentation with Deep Learning on Earth Observation Data: A Review-Part I: Evolution and Recent Trends. *Remote Sensing* **2020**, *12* (10). https://doi.org/10.3390/rs12101667.
22. Hoeser, T.; Bachofer, F.; Kuenzer, C. Object Detection and Image Segmentation with Deep Learning on Earth Observation Data: A Review—Part II: Applications. *Remote Sensing* **2020**, *12* (18). https://doi.org/10.3390/rs12183053.
23. Khelifi, L.; Mignotte, M. Deep Learning for Change Detection in Remote Sensing Images: Comprehensive Review and Meta-Analysis. *IEEE Access* **2020**, *8*, 126385–126400. https://doi.org/10.1109/ACCESS.2020.3008036.
24. Lyu, H.; Lu, H.; Mou, L. Learning a Transferable Change Rule from a Recurrent Neural Network for Land Cover Change Detection. *Remote Sensing* **2016**, *8* (6), 506. https://doi.org/10.3390/rs8060506.
25. Ienco, D.; Gaetano, R.; Dupaquier, C.; Maurel, P. Land Cover Classification via Multitemporal Spatial Data by Deep Recurrent Neural Networks. *IEEE Geoscience and Remote Sensing Letters* **2017**, *14* (10), 1685–1689. https://doi.org/10.1109/LGRS.2017.2728698.
26. Rußwurm, M.; Körner, M. *Temporal Vegetation Modelling Using Long Short-Term Memory Networks for Crop Identification from Medium-Resolution Multi-Spectral Satellite Images*.
27. Zhong, L.; Hu, L.; Zhou, H. Deep Learning Based Multi-Temporal Crop Classification. *Remote Sensing of Environment* **2019**, *221*, 430–443. https://doi.org/10.1016/j.rse.2018.11.032.
28. Mou, L.; Bruzzone, L.; Zhu, X. X. Learning Spectral-Spatial-Temporal Features via a Recurrent Convolutional Neural Network for Change Detection in Multispectral Imagery. *IEEE Transactions on Geoscience and Remote Sensing* **2019**, *57* (2), 924–935. https://doi.org/10.1109/TGRS.2018.2863224.
29. Asner, G. P.; Tupayachi, R. Accelerated Losses of Protected Forests from Gold Mining in the Peruvian Amazon. *Environmental Research Letters* **2016**, *12* (9), 094004. https://doi.org/10.1088/1748-9326/aa7dab.
30. Dethier, E. N. ; S. M. F. L. E. ; E. J. C. ; A. S. P. P. V. ; L. D. Operation Mercury: Impacts of National-Level Military-Based Enforcement Strategy and COVID-19 on Artisanal Gold Mining and Water Quality in a Biodiversity Hotspot in the Peruvian Amazon.
31. Mou, L.; Bruzzone, L.; Zhu, X. X. Learning Spectral-Spatial-Temporal Features via a Recurrent Convolutional Neural Network for Change Detection in Multispectral Imagery. *IEEE Transactions on Geoscience and Remote Sensing* **2019**, *57* (2), 924–935. https://doi.org/10.1109/TGRS.2018.2863224.
32. Drusch, M.; del Bello, U.; Carlier, S.; Colin, O.; Fernandez, V.; Gascon, F.; Hoersch, B.; Isola, C.; Laberinti, P.; Martimort, P.; Meygret, A.; Spoto, F.; Sy, O.; Marchese, F.; Bargellini, P. Sentinel-2: ESA's Optical High-Resolution Mission for GMES Operational Services. *Remote Sensing of Environment* **2012**, *120*. https://doi.org/10.1016/j.rse.2011.11.026.
33. Cordeiro, M. C. R.; Martinez, J. M.; Peña-Luque, S. Automatic Water Detection from Multidimensional Hierarchical Clustering for Sentinel-2 Images and a Comparison with Level 2A Processors. *Remote Sensing of Environment* **2021**, *253*. https://doi.org/10.1016/j.rse.2020.112209.
34. Pahlevan, N.; Smith, B.; Schalles, J.; Binding, C.; Cao, Z.; Ma, R.; Alikas, K.; Kangro, K.; Gurlin, D.; Hà, N.; Matsushita, B.; Moses, W.; Greb, S.; Lehmann, M. K.; Ondrusek, M.; Oppelt, N.; Stumpf, R. Seamless Retrievals of Chlorophyll-a from Sentinel-2 (MSI) and Sentinel-3 (OLCI) in Inland and Coastal Waters: A Machine-Learning Approach. *Remote Sensing of Environment* **2020**, *240*. https://doi.org/10.1016/j.rse.2019.111604.

35. Chan, R. H.; Kan, K. K.; Nikolova, M.; Plemmons, R. J. A Two-Stage Method for Spectral–Spatial Classification of Hyperspectral Images. *Journal of Mathematical Imaging and Vision* **2020**, *62* (6–7), 790–807. https://doi.org/10.1007/s10851-019-00925-9.
36. Peng, D.; Zhang, Y.; Guan, H. End-to-End Change Detection for High Resolution Satellite Images Using Improved UNet++. *Remote Sensing* **2019**, *11* (11). https://doi.org/10.3390/rs11111382.
37. Chen, L.; Zhang, D.; Li, P.; Lv, P. Change Detection of Remote Sensing Images Based on Attention Mechanism. *Computational Intelligence and Neuroscience* **2020**, *2020*, 1–11. https://doi.org/10.1155/2020/6430627.
38. Melgani, F.; Bruzzone, L. Classification of Hyperspectral Remote Sensing Images with Support Vector Machines. *IEEE Transactions on Geoscience and Remote Sensing* **2004**, *42* (8). https://doi.org/10.1109/TGRS.2004.831865.
39. Camps-Valls, G.; Bruzzone, L. Kernel-Based Methods for Hyperspectral Image Classification. *IEEE Transactions on Geoscience and Remote Sensing* **2005**, *43* (6). https://doi.org/10.1109/TGRS.2005.846154.
40. Camps-Valls, G.; Gomez-Chova, L.; Muñoz-Marí, J.; Vila-Francés, J.; Calpe-Maravilla, J. Composite Kernels for Hyperspectral Image Classification. *IEEE Geoscience and Remote Sensing Letters* **2006**, *3* (1). https://doi.org/10.1109/LGRS.2005.857031.
41. Rotaru, C.; Graf, T.; Zhang, J. Color Image Segmentation in HSI Space for Automotive Applications. *Journal of Real-Time Image Processing* **2008**, *3* (4). https://doi.org/10.1007/s11554-008-0078-9.
42. Paschos, G. Perceptually Uniform Color Spaces for Color Texture Analysis: An Empirical Evaluation. *IEEE Transactions on Image Processing* **2001**, *10* (6). https://doi.org/10.1109/83.923289.
43. Cardelino, J.; Caselles, V.; Bertalmío, M.; Randall, G. A Contrario Selection of Optimal Partitions for Image Segmentation. *SIAM Journal on Imaging Sciences* **2013**, *6* (3). https://doi.org/10.1137/11086029X.
44. Cai, X.; Chan, R.; Nikolova, M.; Zeng, T. A Three-Stage Approach for Segmenting Degraded Color Images: Smoothing, Lifting and Thresholding (SLaT). *Journal of Scientific Computing* **2017**, *72* (3). https://doi.org/10.1007/s10915-017-0402-2.
45. Schölkopf, B.; Smola, A. J.; Williamson, R. C.; Bartlett, P. L. New Support Vector Algorithms. *Neural Computation* **2000**, *12* (5). https://doi.org/10.1162/089976600300015565.
46. Hsu, C. W.; Lin, C. J. A Comparison of Methods for Multiclass Support Vector Machines. *IEEE Transactions on Neural Networks* **2002**, *13* (2). https://doi.org/10.1109/72.991427.
47. Binol, H.; Plotner, A.; Sopkovich, J.; Kaffenberger, B.; Niazi, M. K. K.; Gurcan, M. N. Ros-NET: A Deep Convolutional Neural Network for Automatic Identification of Rosacea Lesions. *Skin Research and Technology* **2020**, *26* (3). https://doi.org/10.1111/srt.12817.
48. Dozat, T. *Workshop Track-ICLR 2016 INCORPORATING NESTEROV MOMENTUM INTO ADAM.*
49. Tato, A.; Nkambou, R. Improving ADAM Optimizer. In *Workshop track-ICLR 2018* ; 2018.
50. Information Systems and Wake Forest University. WFU High Performance Computing Facility https://doi.org/10.57682/g13z-2362 (accessed 2022 -02 -27). https://doi.org/10.57682/G13Z-2362.
51. Cohen, J. A Coefficient of Agreement for Nominal Scales. *Educational and Psychological Measurement* **1960**, *20* (1), 37–46. https://doi.org/10.1177/001316446002000104.
52. Jaccard, P. Distribution de La Flore Alpine Dans Le Bassin Des Dranses et Dans Quelques Regions Voisines. *Bulletin de la Société Vaudoise des Sciences Naturelles* **1901**, *37*, 241–272.
53. Dice, L. R. Measures of the Amount of Ecologic Association Between Species. *Ecology* **1945**, *26* (3). https://doi.org/10.2307/1932409.

54. Sørensen, T. A Method of Establishing Groups of Equal Amplitude in Plant Sociology Based on Similarity. *Kongelige Danske Videnskabernes Selskab Biologiske Skrifter* **1948**, *5* (4).
55. Lyapustin, A. I.; Wang, Y.; Laszlo, I.; Hilker, T.; G.Hall, F.; Sellers, P. J.; Tucker, C. J.; Korkin, S. v. Multi-Angle Implementation of Atmospheric Correction for MODIS (MAIAC): 3. Atmospheric Correction. *Remote Sensing of Environment* **2012**, *127*. https://doi.org/10.1016/j.rse.2012.09.002.
56. Claverie, M.; Ju, J.; Masek, J. G.; Dungan, J. L.; Vermote, E. F.; Roger, J. C.; Skakun, S. v.; Justice, C. The Harmonized Landsat and Sentinel-2 Surface Reflectance Data Set. *Remote Sensing of Environment* **2018**, *219*. https://doi.org/10.1016/j.rse.2018.09.002.
57. Vermote, E.; Justice, C.; Claverie, M.; Franch, B. Preliminary Analysis of the Performance of the Landsat 8/OLI Land Surface Reflectance Product. *Remote Sensing of Environment* **2016**, *185*. https://doi.org/10.1016/j.rse.2016.04.008.
58. Masek, J. G.; Vermote, E. F.; Saleous, N. E.; Wolfe, R.; Hall, F. G.; Huemmrich, K. F.; Gao, F.; Kutler, J.; Lim, T. K. A Landsat Surface Reflectance Dataset for North America, 1990-2000. *IEEE Geoscience and Remote Sensing Letters* **2006**, *3* (1). https://doi.org/10.1109/LGRS.2005.857030.
59. Tai, Y. W.; Jia, J.; Tang, C. K. Local Color Transfer via Probabilistic Segmentation by Expectation-Maximization. In *Proceedings - 2005 IEEE Computer Society Conference on Computer Vision and Pattern Recognition, CVPR 2005*; 2005; Vol. I. https://doi.org/10.1109/CVPR.2005.215.
60. Bruzzone, L.; Prieto, D. F.; Serpico, S. B. A Neural-Statistical Approach to Multitemporal and Multisource Remote-Sensing Image Classification. *IEEE Transactions on Geoscience and Remote Sensing* **1999**, *37* (3), 1350–1359. https://doi.org/10.1109/36.763299.
61. Wiratama, W.; Lee, J.; Sim, D. Change Detection on Multi-Spectral Images Based on Feature-Level U-Net. *IEEE Access* **2020**, *8*, 12279–12289. https://doi.org/10.1109/ACCESS.2020.2964798.
62. Chen, H.; Wu, C.; Du, B.; Zhang, L.; Wang, L. Change Detection in Multisource VHR Images via Deep Siamese Convolutional Multiple-Layers Recurrent Neural Network. *IEEE Transactions on Geoscience and Remote Sensing* **2020**, *58* (4), 2848–2864. https://doi.org/10.1109/TGRS.2019.2956756.
63. Kartal, H.; Alganci, U.; Sertel, E. Histogram Matching Based Mosaicking of SPOT 6/7 Satellite Images. In *Proceedings of 9th International Conference on Recent Advances in Space Technologies, RAST 2019*; 2019. https://doi.org/10.1109/RAST.2019.8767868.
64. Wieland, M.; Martinis, S. Large-Scale Surface Water Change Observed by Sentinel-2 during the 2018 Drought in Germany. *International Journal of Remote Sensing* **2020**, *41* (12), 4742–4756. https://doi.org/10.1080/01431161.2020.1723817.
65. Zeng, Y.; Yang, X.; Fang, N.; Shi, Z. Large-Scale Afforestation Significantly Increases Permanent Surface Water in China's Vegetation Restoration Regions. *Agricultural and Forest Meteorology* **2020**, *290*, 108001. https://doi.org/10.1016/j.agrformet.2020.108001.
66. Ji, L.; Gong, P.; Wang, J.; Shi, J.; Zhu, Z. Construction of the 500-m Resolution Daily Global Surface Water Change Database (2001–2016). *Water Resources Research* **2018**, *54* (12). https://doi.org/10.1029/2018WR023060.
67. Shao, P.; Shi, W.; He, P.; Hao, M.; Zhang, X. Novel Approach to Unsupervised Change Detection Based on a Robust Semi-Supervised FCM Clustering Algorithm. *Remote Sensing* **2016**, *8* (3). https://doi.org/10.3390/rs8030264.
68. Liu, S.; Marinelli, D.; Bruzzone, L.; Bovolo, F. A Review of Change Detection in Multitemporal Hyperspectral Images: Current Techniques, Applications, and Challenges. *IEEE Geoscience and Remote Sensing Magazine*. 2019. https://doi.org/10.1109/MGRS.2019.2898520.

69. Liu, S.; Du, Q.; Tong, X.; Samat, A.; Bruzzone, L.; Bovolo, F. Multiscale Morphological Compressed Change Vector Analysis for Unsupervised Multiple Change Detection. *IEEE Journal of Selected Topics in Applied Earth Observations and Remote Sensing* **2017**, *10* (9). https://doi.org/10.1109/JSTARS.2017.2712119.
70. Maggioni, M.; Murphy, J. M. Learning by Unsupervised Nonlinear Diffusion. *Journal of Machine Learning Research* **2019**, *20*.
71. Murphy, J. M.; Maggioni, M. Unsupervised Clustering and Active Learning of Hyperspectral Images with Nonlinear Diffusion. *IEEE Transactions on Geoscience and Remote Sensing* **2019**, *57* (3). https://doi.org/10.1109/TGRS.2018.2869723.
72. Polk, S. L.; Murphy, J. M. Multiscale Clustering of Hyperspectral Images Through Spectral-Spatial Diffusion Geometry; 2021. https://doi.org/10.1109/igarss47720.2021.9554397.